Supporting Information for "Moulin density controls the timing of peak pressurization within the Greenland Ice Sheet's subglacial drainage system"

J. Z. Mejia[1], J. D. Gulley[2], C. Trunz[3], M. D. Covington[4], T. C. Bartholomaus[5], C. Breithaupt[6], S. Xie[7], T. H. Dixon[2]

[1]Department of Geology, University at Buffalo, Buffalo, NY 14260
[2]Department of Geosciences, University of South Florida, Tampa, FL 33620.
[3]Department of Applied Geomatics, Université de Sherbrooke, Sherbrooke, QC J1K 2R1, Canada
[4]Department of Geosciences, University of Arkansas, Fayetteville, AR 72701
[5]Department of Earth and Spatial Sciences, University of Idaho, Moscow, ID 83844
[6]Exxonmobil Upstream Research Company, Spring, TX 77389
[7]Department of Civil and Environmental Engineering, University of Houston, Houston, TX 77204

Supplement Contents

Introduction

This supplement provides additional information relating to the main text and details on methodology. **Text S1** describes the characteristics of the catchments studied at Low Camp and High Camp. **Text S2** describes the methodology used to delineate catchment boundaries and calculate each catchment's area. **Text S3** details our meteorological measurements and the model used to calculate meltwater production. **Text S4** details our measurements of supraglacial stream stage and discusses stream discharge measurements that we report in **Table S3**. In **Text S5** we provide more details on moulin instrumentation. **Text S6** explains the methodology used in post-processing GNSS station data and calculating surface ice velocity. **Text S7** details the analysis of seismic data to resolve glaciohydraulic tremor amplitude. **Text S8** discusses how we identified diurnal extrema values across our timeseries data sets using the `DiurnalExtrema` python module developed for this study. Finally, **Text S9** elaborates on how diurnal extrema timing changes over the course of the 2018 melt season at our lower elevation site.

Text S1. Catchment characteristics

We instrumented a total of three moulins during this study. At Low Camp, we instrumented moulins draining the same catchment (0.2 km^2 area) in both the 2017 and 2018 melt seasons. We instrumented moulin JEME on 20 July 2017 and moulin PIRA on 10 July 2018. PIRA moulin formed by a crevasse cross-cutting the supraglacial stream feeding JEME moulin after it was advected approximately 90 m downglacier (Figure S3). By instrumenting PIRA moulin, we measured water pressures in the same region of the subglacial drainage system in both years. Low Camp has a high moulin density with at least eight other moulins within a 1 km radius of moulin JEME and PIRA in 2017 and 2018 (Figure S4). Additionally, there are two crevasse fields within 2 km of our instrumented moulins, one to the east and the other to the southwest. We instrumented Radical (RADI) moulin at High Camp during the 2017 melt season. Radical moulin drained a catchment with an area of ~ 16.6 km^2. High Camp had a much lower moulin density with one moulin within a 1 km radius of RADI moulin with a single crevasse located approximately 250 m downglacier (Figure S5).

Text S2. Catchment delineation

To delineate internally drained catchments, we corrected automatically determined boundaries by visual inspection of remote sensing imagery. We use ArcticDEM mosaic with a ground sample distance of two meters (Porter et al., 2018) derived from the panchromatic bands of WorldView satellites in the DigitalGlobe optical imaging constellation. We project the DEMs into the WGS84 / NSIDC Sea Ice Polar Stereographic North coordinate reference system (EPSG:3413). This Polar Stereographic projection is based on the World Geodetic System 1984 ellipsoid (WGS84). We performed the following steps to delineate supraglacial catchments from the DEM mosaic: First, we applied an algorithm to identify and fill topographic sinks (Conrad et al., 2015; Wang & Liu, 2006) while preserving the downward slope of the flow path (i.e., the minimum slope gradient between cells). Then we used the created depressionless DEM to calculate supraglacial flow accumulation via the steepest descent algorithm (flow into and out of each grid element). This methodology produces a shapefile of predicted supraglacial stream locations. By prescribing moulin locations we are then able to define supraglacial catchment boundaries. We then manually inspect these predicted catchment boundaries by comparing them to high-resolution WorldView imagery. Where mismatches between catchment boundaries and actual supraglacial flow paths are

0094-8276/22/$5.00

identified, we adjust the catchment polygon to reflect the actual stream routing locations.

Text S3. Meteorological measurements

To quantify the timing and magnitude of surface melting we installed automatic weather stations at our lower and higher elevation field sites. The LOWC weather station was installed at Low Camp (69.4727°N, 49.8263°W, 780 m.a.s.l.) on 2 July and the HIGH weather station was installed at High Camp (69.5416°N, 49.7100°W, 950 m.a.s.l.) on 28 July 2017 (Mejia, Trunz, Covington, & Gulley, 2020). Each weather station was equipped with a Onset ®HOBO ®U30-NRC data logger mounted onto aluminum conduit frozen into the ice that recorded meteorologic measurements every 15 minutes. The 10 Ahr battery powering each logger was recharged by a 5 W solar panel. Peripheral sensors were mounted above the data logger so that they were ~ 2 m above the ice surface at the time of instillation. Air temperature was measured using an air temperature and relative humidity smart sensor installed within a solar radiation shield. We measured incoming and reflected shortwave solar radiation using two silicon pyranometers mounted onto a bracket that extended the sensors 42 cm from the station's mast. Incoming radiation was measured by our upward pointing sensor and reflected radiation was measured by our downward pointing sensor.

The HOBO/Onset weather stations deployed at our (LOWC) Low Camp and (HIGH) High Camp field sites recorded air temperature, incoming and outgoing solar radiation, along with other measurements, at 15 minute intervals. We use meteorological measurements from the GC-NET weather station JAR1 to fill in data gaps. We calculate melt rate M with units of (mm w.e. h^{-1}) from air temperature T and incoming shortwave radiation G measurements for each weather station using an enhanced temperature-index melt model (Pellicciotti et al., 2005):

$$M = \begin{cases} TF\mathrm{T} + SRF(1-\alpha)\mathrm{G} & \text{if } \mathrm{T} > \mathrm{T}_T \\ 0 & \text{if } \mathrm{T} \geq \mathrm{T}_T \end{cases} \quad (1)$$

where TF is a temperature factor (TF=0.05 mm h^{-1} $°C^{-1}$), SRF is a shortwave radiation factor (SRF=0.0094 m^2 mm W^{-1} h^{-1}), α is daily ice surface albedo, and T_T is a threshold temperature taken to be 0°C under which no melting occurs (Mejia, Trunz, Covington, & Gulley, 2020).

Incoming shortwave radiation measurements were corrected for errors resulting from shadows cast on the weather station. The drop in solar radiation caused by the shadow is systematic, occurring between 11:00–13:00 UTC though the melt season. We applied a multidimensional median filter to the incoming solar radiation timeseries to account for these errors. Daily albedo values were determined using incoming and reflected solar radiation measurements from 15:00 UTC, when incoming solar radiation is at its peak and the solar zenith angle (θ) is less than 50° (Pellicciotti et al., 2005). In 2018, only one solar radiation sensor was functional upon return to our LOWC weather station, we used that sensor to record incoming solar radiation. As such, we were unable to calculate daily albedo values and instead use a constant value of 0.7 for all 2018 melt rate calculations. The timing of peak daily melt is unaffected by this choice of albedo.

Ice surface ablation was monitored by our stream gauging stations (Figure S1c) during the 2017 and 2018 melt seasons using a Global Water Ultrasonic distance sensor WL705-012. The sensors were affixed to aluminum conduit frozen into the ice surface via a steel extension arm. This sensor was powered and controlled by the stream gauging station's Campbell Scientific CR1000 data logger which recorded measurements every 15-minutes. We compare melt rate calculated using Equation 1 to our observations of ice surface lowering and find good agreement in magnitude (Figure S6) and in timing (Figures S7 and S8) for coincident measurements between 13 July through 19 August 2017. Figure S6 shows the observed surface lowering measurements converted to water equivalent using various ice densities. We find that using an average ice density of 0.7 g cm^{-3} produces the best fit to calculated melt rates. Hourly ice surface ablation is compared to calculated melt rate and air temperatures in Figure S7 and the diurnal extrema picks are shown in Figure S8. Calculated peak melting occurred on average at 13:30±1.0 hours (n = 37), agreeing with ablation measurements which show an average peak at 13:30±3.4 hours (n = 20). We also find that air temperature peaks two hours later than melting, occurring at 15:30±3.3 hours (n = 35).

Text S4. Supraglacial stream stage and discharge measurements

We monitor the timing of meltwater delivery to moulins by measuring the water level (or stream stage) of supraglacial streams just upstream their terminal moulins. We installed gauging stations ~ 30 m upstream of each stream's terminal moulin. Each gauging station was equipped with a Global Water ultrasonic water level sensor (model WL705-048 or WL705-012) affixed to a self-lowering crossbar mounted on either side of the supraglacial stream (Figures S1–S2). Campbell Scientific CR1000 data loggers equipped with DCDC-18R voltage boost regulators supplied power to the ultrasonic water level sensors. Data loggers were programmed to power on the water level sensor every 15 minutes and record the distance to the water's surface following a 15 second stabilization period. This 15 second averaging window reduces the influence of turbulence on the water level measurement. We use 100 Ω current shunt modules to convert the current output by the ultrasonic water level sensor into a voltage that can be measured by the data logger. We determine stream stage using an arbitrary datum of four meters below the face of each ultrasonic water level sensor. We use these measured water level fluctuations to constrain the timing of peak meltwater delivery to moulins (i.e., peak daily stream water level).

We measured the stage for the supraglacial streams draining into instrumented moulins during 2017 and 2018 (Tables S1 and S2). In 2017 we measured stream stage within the supraglacial streams terminating into JEME moulin at Low Camp and RADI moulin at High Camp. During the 2018 melt season, we monitored stream stage within JEME catchment at Low Camp. To better constrain the influence of catchment area on the timing of meltwater delivery to moulins we measured stream stage at two auxiliary sites near each camp—a catchment named JNIH near Low Camp and SBPI near High Camp (Figure 1). The catchment JNIH has an area of 1.1 km^2, and SBPI catchment has an area of 2.4 km^2 (Table S3). The average timing of peak meltwater delivery to the moulins draining these auxiliary catchments is shown in Figure 2a.

Supraglacial stream discharge: We collected point measurements of supraglacial stream discharge using two methods: (1) constant rate tracer injection method and (2) by using a continuous wave Doppler. In 2017 we used dye injection exclusively whereas in 2018 we used a combination of the two methods which are explained in detail below. We use the point measurements of stream discharge to calibrate a simple unit hydrograph model so that we can compare all of the instrumented catchments without incorporating biases deriving from measurement length, melt intensity, or timing within the melt season.

During the 2017 melt season, we measured stream discharge using the constant rate tracer injection method (Kilpatrick & Cobb, 1985). A known concentration (200 or 40 ppb) of Rhodamine dye was injected at a rate of 2 ± 0.5 mL per minute using a peristatic pump into into each stream 50–100 upstream of a Turner Cyclops-7 submersible fluorometer that measured dye concentration every three seconds. The distance between the dye injection point and fluorometer exceeded 200 stream widths, allowing the dye to fully mix within the water column. Stream discharge (Q, $m^3 s^{-1}$) can then be calculated using:

$$Q = q\left(\frac{C_1}{C_2}\right) \tag{2}$$

where q is the rate of tracer injection into the supraglacial stream, C_1 is the concentration of the Rhodamine dye injection solution (mg L^{-1}), and C_2 is the fluorometer measured dye concentration. We estimated the error of measurements to be ±25% due to small variations in pump rate (1.5–2.5 ml s^{-1}).

During the 2018 melt season we incorporated the use of a Teledyne ISCO 2150 Area Velocity Flow Module to measure supraglacial stream discharge. This instrument measures stream level and average stream velocity to calculate the volume and rate of flow within open-channel streams. The instrument's Area Velocity (AV) sensor is mounted on the base of the supraglacial stream. The AV sensor is equipped with a piezo-resistive transducer that measures the liquid level above the stream's base. Water level calculations consider current atmospheric pressure through an internal vent tube that connects to the AV module on the ice surface. The produced water level measurements have an accuracy of 0.003 m, and a typical long term stability of ±0.007 m yr^{-1} The AV sensor also measures flow velocity by using the Doppler effect and ultrasonic sound waves (error of ±0.03 m s^{-1} or ±2% of reading). The pair of ultrasonic transducers located within the sensor emit and receive sound waves. The emitted and received wave frequency is then compared to determine flow velocity because the degree of change is proportional to the stream's velocity. We use these measurements in conjunction with a measured profile of the supraglacial stream to calculate the volume of water flowing into the stream's terminal moulin. We used a U-shape for PIRA stream with one meter width, and a rectangular shape for SBPI stream with a 10.4 m width.

Point measurements of stream discharge were compared to yield the average values reported in (Table S3) by using the Synthetic Unit Hydrograph (SUH) (King, 2018; Smith et al., 2017). The SUH curve calculates moulin discharge q (hr^{-1}) at time t using:

$$q(t) = e^m \left[\frac{t}{t_p}\right]^m \left[e^{-m\left(\frac{t}{t_p}\right)}\right] h_p \tag{3}$$

where m is the equation shape factor, t_p is time to peak discharge in hour (our measured lag time between peak melting and peak stream discharge), and h_p is peak discharge (hr^{-1}). We estimate hourly moulin hydrographs by convolving hourly melt data (M) with the SUH produced q-curve.

$$Q = M * q \tag{4}$$

here, $*$ is the convolution operator that we implement using NumPy's `convolve` function. The full SUH calculation is available in the Jupyter Notebook `calcSUH.ipynb` archived with Arctic Data (see Trunz et al., 2021).

Text S5. Moulin instrumentation

We instrumented a total of three moulins during the 2017 and 2018 melt seasons after the snowline retreated past each field site. At Low Camp, we instrumented moulin JEME on 20 July 2017 and moulin PIRA the following melt season on 10 July 2018. PIRA moulin formed by a crevasse crosscutting the supraglacial stream feeding JEME moulin after it was advected approximately 90 m downglacier (Figure S3). By instrumenting PIRA moulin, we measured water pressures in the same region of the subglacial drainage system in both years. At High Camp, we initially instrumented RADI moulin on 29 July 2017 (Mejia, Gulley, & Dixon, 2020). We used the same equipment and methodology to instrument all moulins in both years.

Moulin instrumentation was preformed using the following procedure. Geokon 4500-HD piezometers affixed to armored cable was lowered into moulins by measured lengths to constrain the distance from the ice-surface to the water column within each moulin. Campbell Scientific CR1000 data logger readings indicated that during the lowering process we encountered points where lowering additional cable did not increase the piezometer's reported submerged depth. We anchored the piezometers at the ice surface just above these elevations within the moulins, initially resulting in a truncated timeseries whenever water level fell below the sensor's submerged depth. In 2017 we were able to further lower the piezometer following the initial installation (on 23 July for JEME moulin and 6 August for RADI moulin) allowing us to record the full range of daily water level fluctuations within JEME and RADI moulins. After installation Campbell data loggers were programmed to record water level readings every 15 minutes.

Piezometric measurements of water pressure (P_w) were converted to hydraulic head (h) with the assumption of a vertical moulin shaft following:

$$h = \frac{P_w}{\rho_w g} + z_{sensor} \tag{5}$$

where ρ_w is the density of water, g is acceleration due to gravity, and z_{sensor} is the piezometer's elevation in meters above sea level. In 2017 we were able to correct our measurements of moulin hydraulic head for atmospheric pressure variability recorded at the GC-NET weather station JAR1. Due to instrument failure we were not able to correct our 2018 observations. Fortunately, the uncertainty added by the lack of atmospheric pressure correction is small (on the order of centimeters) compared to diurnal moulin water level variability (on the order of tens of meters). A comparison of corrected and uncorrected moulin hydraulic head timeseries for the 2017 melt season is shown in Figure S2 of Mejia et al. (2021).

Text S6. GNSS data processing

We use data acquired from four on-ice Global Navigation Satellite System (GNSS) stations to capture the ice-dynamic response to meltwater inputs to moulin-connected drainage systems at both of our field sites (Mejia, Trunz, Covington, Gulley, & Breithaupt, 2020). GNSS station JEME was co-located with moulin JEME in 2017 and moulin PIRA in 2018, and station RADI was co-located with RADI moulin in 2017. We use measurements from nearby stations to fill gaps in our timeseries. We used TRACK software, which utilizes carrier-phase differential processing relative to bedrock mounted base stations. We use base station KAGA with a ~ 28 km baseline length (Fahnestock et al., 2006)and station

ROCK with a ~ 36 km baseline length (Mejia, Trunz, Covington, Gulley, & Breithaupt, 2020) to determine kinematic site positions of our on-ice GNSS stations (Herring et al., 2010; Xie et al., 2019). We transform station positions to the along-flow direction and apply a centered 6 hour moving average filter to reduce noise while preserving diurnal variability, using this timeseries to calculate ice velocities. By centering this filter with respect to time, we maintain the timing of velocity extrema as has been previously demonstrated (e.g., ?, ?; Mejia et al., 2021).

Text S7. Seismic glaciohydraulic tremor

To further characterize water flow within the subglacial drainage system, we installed the seismic station SELC nearby JEME catchment before the melt season began in April 2018. The amplitude of glaciohydraulic tremor depends on the flux and pressure gradient of turbulent water flowing within well-connected subglacial conduits (Bartholomaus et al., 2015; Gimbert et al., 2016). Seismic station SELC was equipped with a Nanometrics Centaur digitizer and a Nanometrics Trillium compact posthole sensor that was covered in sand to improve sensor-ice coupling. The raw, recorded waveforms were corrected for their instrument responses. We determined glaciohydraulic tremor amplitude as the 20th percentile amplitude of 10 minute, enveloped, vertical, velocity seismic waveforms, high-pass filtered above 2 Hz (see Mejia et al., 2021, for more details). See Röösli et al. (2014) a more thorough discussion of the differences in seismic signals associated with other seismic sources—shallow and deep icequakes, and long duration (> 30 minute) tremor from moulin activity—that we do not consider in this study.

Text S8. Diurnal extrema picks

We determined diurnal extrema values from timeseries observations using the `DiurnalExtrema` python module created for this project. This module determines diurnally varying extrema by implementing specific specifications for local extrema picks. In addition to limiting the number of maximum and minimum extrema picks to one per day (24 hour period), requiring the minimum value precede the maximum, or allowing an extrema to fall outside of the 24 hour calendar day. This module is open-source and can be accessed through GitHub or Zortoro, see the data availability statement following the main text for details.

Figures S9–S11 show timeseries data sets with diurnal extrema picks used to generate the statistics described with the main text, underlying Figures 2 and 4, and reported by Table S3. Data collected at Low Camp during the 2017 melt season is plotted in Figure S9. Supraglacial stream stage shown for the auxiliary catchment JNIH (orange) and our main catchment JEME (blue) (Figure S9b). Because we are only interested in diurnal meltwater propagation, we exclude the spike in stream stage on 24 July 2017 that coincided with a period of heavy rainfall. Spikes in the moulin hydraulic head (Figure S9c) and ice velocity (Figure S9d) on 27 July 2017 were similarly excluded because they were caused by a subglacial floodwave following the rapid draining of upglacier supraglacial lakes rather than by diurnal meltwater inputs to JEME moulin. We recorded a similar event on 25 July 2018 and similarly exclude the dates from extrema picks (Figure S10), and exclude dates corresponding to recorded rainfall.

Text S9. Seasonal evolution

To determine how snowpack removal and increased supraglacial drainage efficiency influence the timing of meltwater delivery to moulins, we explore how lags in meltwater propagation changed throughout the 2018 melt season at Low Camp. Lags between peak melting and all other variables decreased as the melt season progressed (Figure 4), with the most considerable change occurring between June and July. On diurnal timescales, peak tremor amplitude occurs near the time of peak meltwater delivery to PIRA moulin (Figure S13), when subglacial pressure gradients are increasing most rapidly. Between June and July, lags between peak melting and peak tremor amplitude decreased by 3.25 hours. Between June and July, lags between peak melting and peak sliding decreased by 4 hours. These observations likely reflect the removal of the seasonal snowpack as the snowline retreated upglacier as the melt season progressed.

Between July and August lags between peak melting and all other variables decreased. Lags between peak meltwater production and delivery to PIRA moulin decreased by 54 minutes. This change was reflected in the timing of peak moulin water level which occurred 39 minutes earlier in August than in July. Lags between peak melting and peak tremor amplitude decreased by an additional 1.75 hours between July and August, and lags between peak melting and peak sliding speed decreased by one hour.

References

Bartholomaus, T. C., Larsen, C. F., Amundson, J. M., O'Neel, S., Walter, J. I., & West, M. E. (2015). Subglacial discharge at tidewater glaciers revealed by seismic tremor. *Geophysical Research Letters*, *42*, 6391–6398. doi: 10.1002/2015GL064590

Conrad, O., Bechtel, B., Bock, M., Dietrich, H., Fischer, E., Gerlitz, L., ... Böhner, J. (2015). System for Automated Geoscientific Analyses (SAGA) v. 2.1.4. *Geoscientific Model Development*, *8*(7), 1991–2007. doi: 10.5194/gmd-8-1991-2015

Fahnestock, M. A., Truffer, M., SDFE, T. D. A., & Community, U. (2006). *Greenland GNSS Network - KAGA-Kangia North P.S.,*. UNAVCO. doi: 10.7283/FQGY-4535

Gimbert, F., Tsai, V. C., Bartholomaus, T. C., Amundson, J. M., & Walter, J. I. (2016). Subseasonal changes observed in subglacial channel pressure, size, and sediment transport. *Geophysical Research Letters*, *43*(September), 3786–3794. doi: 10.1002/2016GL068337

Herring, T., King, R. W., & McClusky, S. C. (2010). Introduction to GAMIT/GLOBK. *Mass. Inst. of Technol., Cambridge, Mass.*

Kilpatrick, F. A., & Cobb, E. D. (1985). Measurement of discharge using tracers. In *Techniques of water-resources investigations of the united states geological survey* (Vol. Book 3, pp. 1–52).

King, L. A. (2018). *Identifying and characterizing the spatial variability of supraglacial hydrological features on the western Greenland Ice Sheet* (Doctoral dissertation, University of British Columbia). doi: 10.14288/1.0372827

Mejia, J. Z., Gulley, J. D., & Dixon, T. H. (2020). *West Greenland Moulins 2017-2019 Sermeq Avannarleq - GPS/GNSS Observations Dataset.* The GAGE Facility operated by UNAVCO, Inc. doi: 10.7283/VT31-EK40

Mejia, J. Z., Gulley, J. D., Trunz, C., Covington, M. D., Bartholomaus, T. C., Xie, S., & Dixon, T. (2021). Isolated cavities dominate Greenland Ice Sheet dynamic response to lake drainage. *Geophysical Research Letters*, 1–11. doi: 10.1029/2021gl094762

Mejia, J. Z., Trunz, C., Covington, M. D., & Gulley, J. D. (2020). *Meteorological data from two on-ice weather stations at 780 and 950 m asl elevations in the ablation area of Sermeq Avannarleq, West Greenland from 2017-2018.* Arctic Data Center. doi: 10.18739/A2CF9J745

Mejia, J. Z., Trunz, C., Covington, M. D., Gulley, J. D., & Breithaupt, C. (2020). *Moulin hydrological measurements from Sermeq Avannarleq, West Greenland Ice Sheet from 2017-2018.* Arctic Data Center. doi: 10.18739/A2M03XZ13

Pellicciotti, F., Brock, B., Strasser, U., Burlando, P., Funk, M., & Corripio, J. (2005). An enhanced temperature - index glacier melt model including the shortwave radiation balance : development and testing for Haut Glacier d ' Arolla , Switzerland. *Journal of Glaciology*, *51*(175), 573 – 587. doi: 10.3189/172756505781829124

Porter, C., Morin, P., Howat, I., Noh, M.-J., Bates, B., Peterman, K., ... Nakamura, H. (2018). *ArcticDEM.* Harvard Dataverse. doi: http://doi.org/10.7910/DVN/OHHUKH

Röösli, C., Walter, F., Husen, S., Andrews, L. C., Luthi, M. P., Catania, G. A., & Kissling, E. (2014). Sustained seismic tremors and icequakes detected in the ablation zone of the Greenland ice sheet. *Journal of Glaciology*, *60*(221), 563–575. doi: 10.3189/2014JoG13J210

Smith, L. C., Yang, K., Pitcher, L. H., Overstreet, B. T., Chu, V. W., & Rennermalm, Å. K. (2017). Direct measurements of meltwater runoff on the Greenland ice sheet surface. *Proceedings of the National Academy of Sciences*, *114*(50), 1–10. doi: 10.1073/pnas.1707743114

Trunz, C., Mejia, J., Covington, M., Siegel, V., Conlon, B., & Gulley, J. D. (2021). *Supraglacial stream discharge measurements from six catchments within the Pâqitsoq region of Sermeq Avannarleq, western Greenland Ice Sheet 2017 -2018. Arctic Data Center.* Arctic Data Center. doi: 10.18739/A2D21RK53

Wang, L., & Liu, H. (2006). An efficient method for identifying and filling surface depressions in digital elevation models for hydrologic analysis and modelling. *International Journal of Geographical Information Science*, *20*(2), 193–213. doi: 10.1080/13658810500433453

Xie, S., Law, J., Russell, R., Dixon, T. H., Lembke, C., Malservisi, R., ... Chen, J. (2019). Seafloor Geodesy in Shallow Water With GPS on an Anchored Spar Buoy. *Journal of Geophysical Research: Solid Earth*, *124*(11), 12116–12140. doi: 10.1029/2019JB018242

Table S1. Catchment geometry

	Low Camp		High Camp		
Name	JEME[†]	PIRA[†]	JNIH	RADI	SBPI
Instrumented	2017	2018	2017	2017	2018
Area (km^2)	0.24	0.24	1.11	16.77	2.37
Length (km)	1.0	1.0	1.8	7.5	1.7
Elongation ratio[‡]	0.55	0.55	1.05	0.62	1.16
Elevation (m.a.s.l.)	779	779	790	947	927
Ice thickness (m)*	503	503	547	634	732
Moulin instrumented	✓	✓		✓	

[†] PIRA and JEME drained the same catchment. PIRA formed during 2018.
[‡] calculated from the catchment's area A and length L following $Re = (A/\pi)^{0.5}/L$.
* Ice thicknesses derived from BedMachine v3 data.

Table S2. Moulin coordinates

	Latitude °N	Longitude (°W)
JEME PIRA	69.4741	49.8232
JNIH	69.4684	49.8318
SBPI	69.5294	49.7231
RADI	69.5428	49.7029

Table S3. Catchment area, discharge, and lags.

				melt→stage		melt→moulin		melt→sliding	
	Area km^2	Elevation m.a.s.l.	Discharge m^3/s	n	LAG hrs	n	lag hrs	n	LAG hrs
JEME	0.24	779	0.11	7	2.4±1.6	28	5.2±1.3	20	4.4±1.1
PIRA			0.10	3	2.5±1.3	32	4.9±1.5	31	4.8±2.0
JNIH	1.11	790	0.14	5	4.2±1.8			7	4.9±1.8
SBPI	2.37	927	0.45	3	5.0±1.3				
RADI	16.77	947	2.15	11	6.5±1.8	19	7.9±2.2	12	10.5±1.6

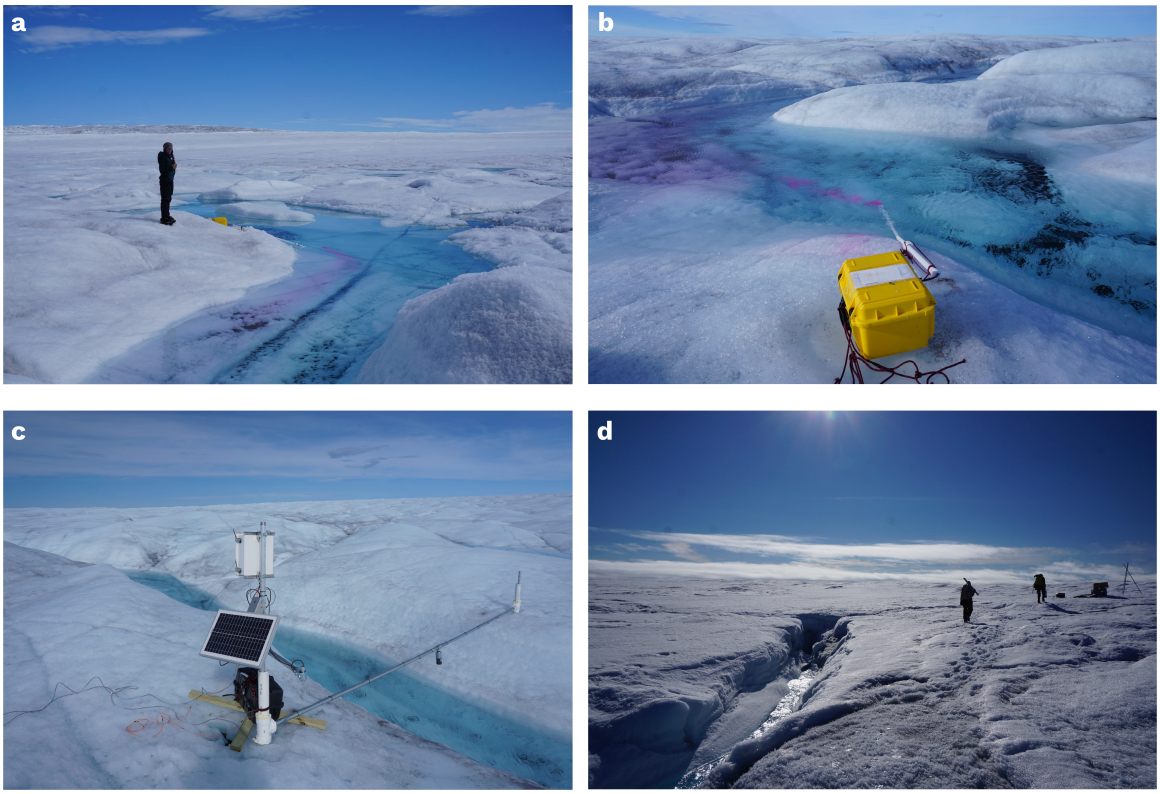

Figure S1. Low Camp supraglacial stream instrumentation. (a–b), Rhodomine dye injection pump positioned several stream widths upstream from our submerged cyclops fluorometer attached to the stream gauging station. (c) Global water WL705-048 ultrasonic water level sensor attached to a self-lowering cross-bar. The instrument was powered by a 12V battery, recharged with a solar panel, also powering the Campbell scientific data logger which recorded stage measurements every 15-minutes. Another ultrasonic range sensor was mounted to a small crossbar near the data logger, positioned downward to measure surface ablation. (d) JNIH moulin, instrumented with a Geokon 4500HD piezometer.

Figure S2. High Camp supraglacial stream instrumentation. (a) Radical (RADI) moulin, instrumented with a Geokon piezometer in mid-July 2017. (b) RADI stream gauging station. Stream stage was measured using the same setup deployed at our Low Camp field sites where a Global Water ultrasonic water level sensor (WL705-012) measured stream stage at 15 minute intervals.

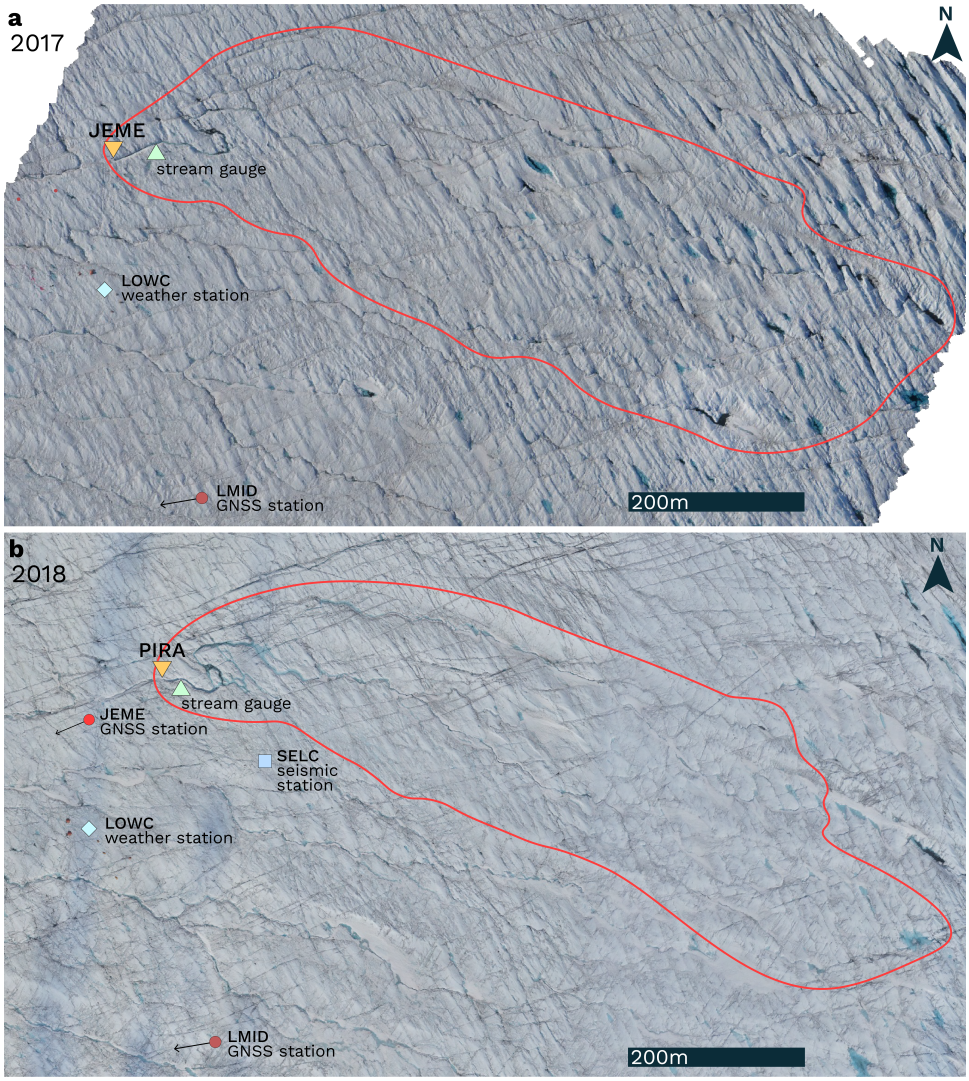

Figure S3. JEME and PIRA moulin and drainage basin comparison. (a), Drone orthoimage from July 2017 showing the location of our instrumented moulin JEME and the bounds of its supraglacial drainage basin. (b) Drone orthoimage from July 2018 showing the location of our instrumented moulin PIRA which opened in the same location as JEME the previous year. The drainage basin is delineated and other instruments are shown along with the ice flow direction in the area (black arrows).

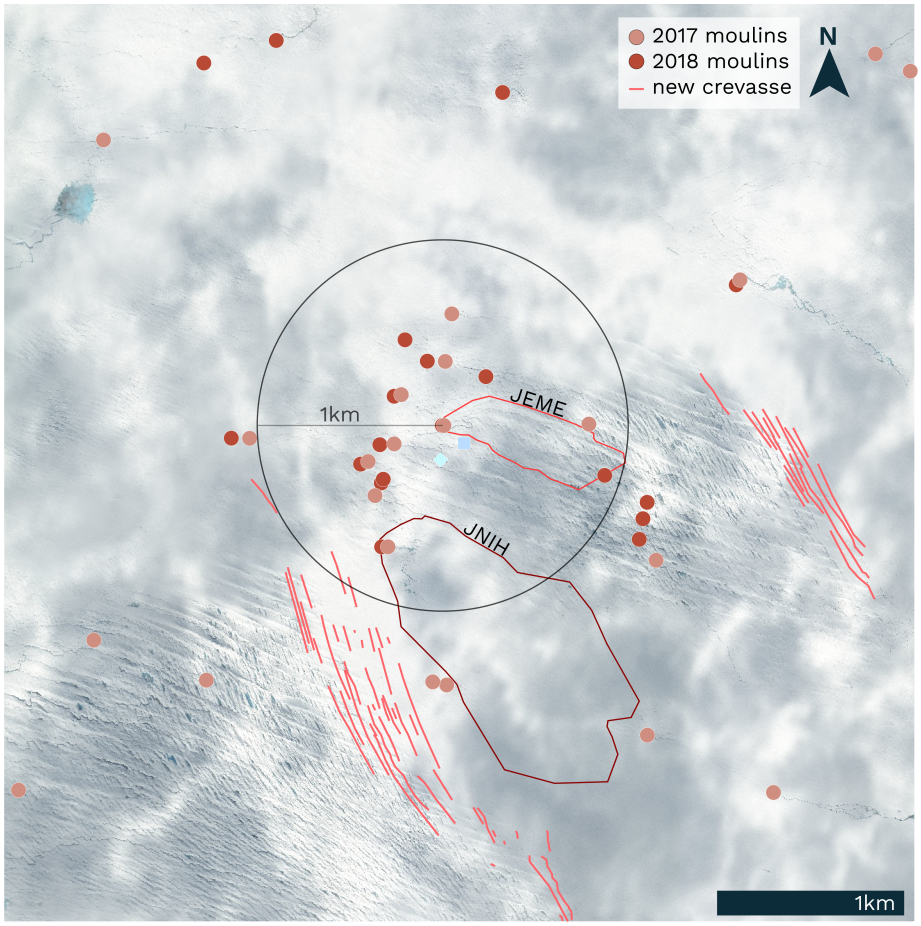

Figure S4. Low Camp moulin and crevasse distribution. WorldView-2 Imagery (copyright 2017 DigitalGlobe Inc.) acquired 03 July 2017. Moulins identified in 2017 (orange) and 2018 (red) are marked by circles. Red lines show newly formed crevasses. JEME and JNIH drainage basins and terminal moulins are also marked and labeled. An area with a 1-km radius centered on JEME/PIRA moulin is shown, representing a diameter of approximately four ice-thicknesses.

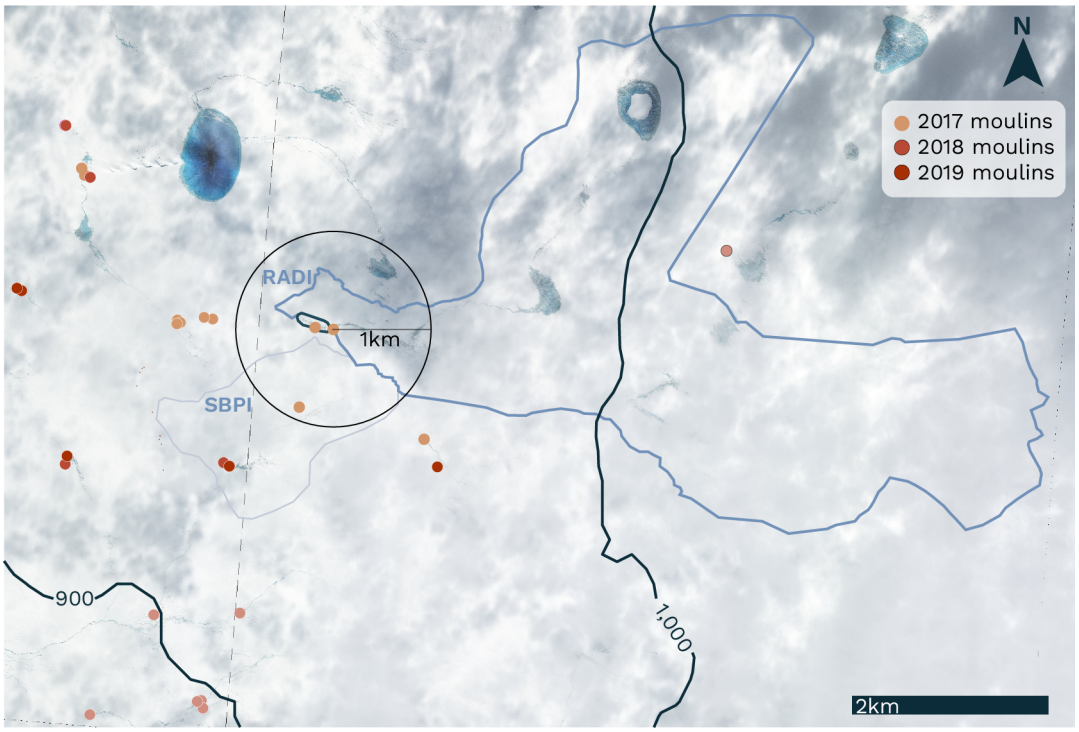

Figure S5. High Camp moulin and crevasse distribution. WorldView-2 Imagery (copyright 2017 DigitalGlobe Inc.) acquired 03 July 2017. Moulins identified in 2017 (orange) and 2018 (red) are marked by circles (2019 darkest). RADI drainage basin, along with SBPI and a small nearby moulin and drainage area are delineated. An area with a 1km radius is centered on RADI moulin, with the diameter representing approximately three ice thicknesses.

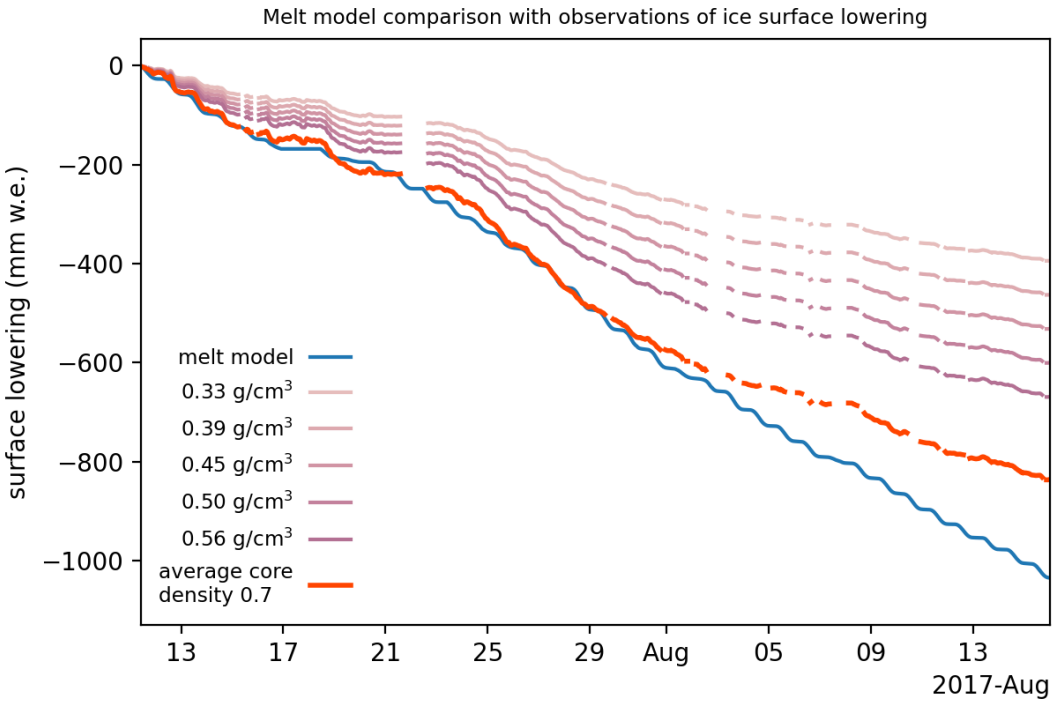

Figure S6. Observed and calculated surface meltwater production comparison for Low Camp, 2017. Modeled surface meltwater production (blue) compared with ice surface ablation measurements converted to mm w.e. using average ice densities ranging from 0.33–0.56 g/cm^3 in purple and the best fit of 0.7 g/cm^3 in red.

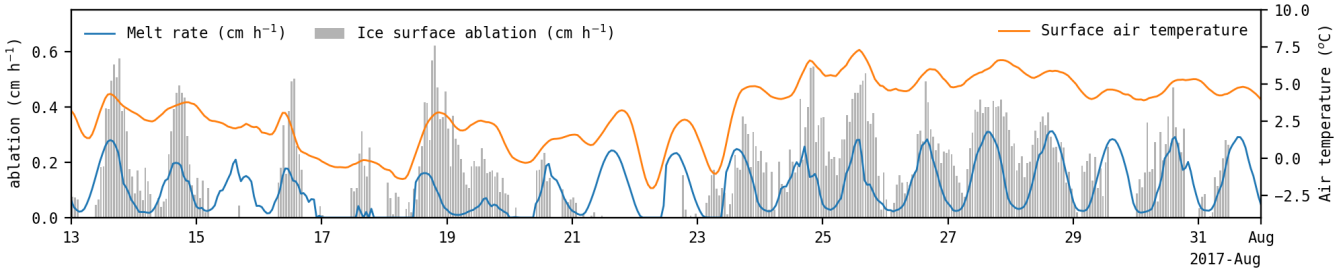

Figure S7. Comparison between hourly surface air temperature (orange), melt rate (blue), and ice surface ablation (gray) recorded at Low Camp during July 2017.

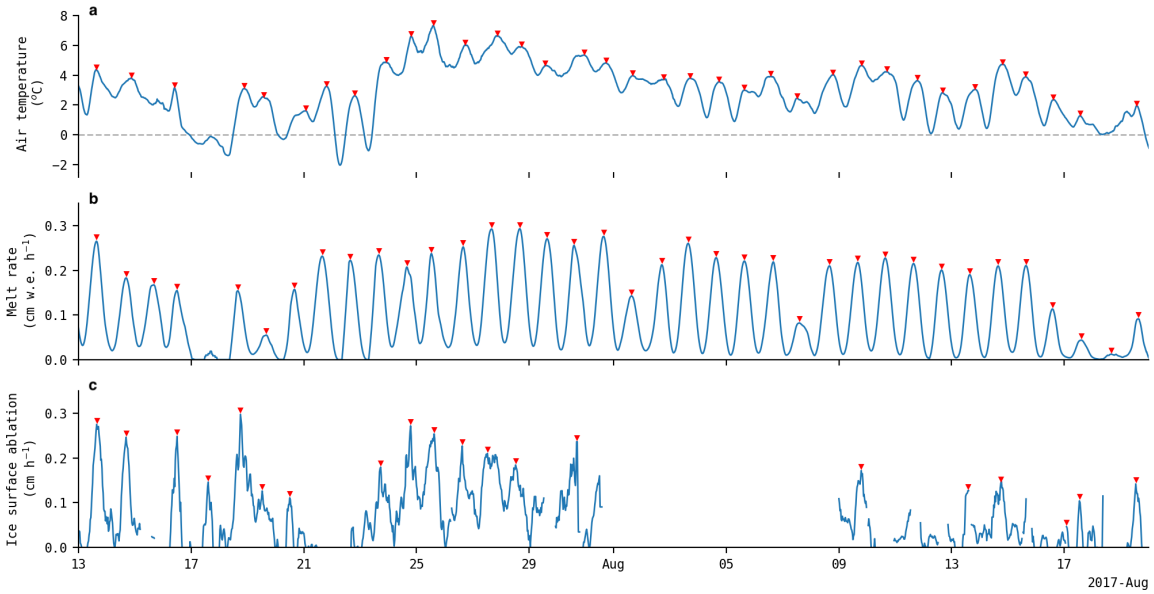

Figure S8. Comparison between diurnal extrema in meteorological measurements from Low Camp, 2017. (a) Surface air temperature measured by LOWC AWS positioned at Low Camp. Diurnal extrema picks used to calculate the average timing of peaks is marked by red triangles. Peak air temperature occurs on average at 15:30±3.3 hours with n = 35. (b) Calculated melt rate determined using meteorological measurements from LOWC AWS. Diurnal peak melt rate occurs at 13:30±1.0 hours where n = 37. (c) Hourly ice surface ablation measured at the JEME gauging station at Low Camp in 2017. A two hour smoothing window is applied and we ignore dates where our instrument did not capture the entire range of diurnal variability. Peak ice surface ablation occurred on average at 13:30±3.4 hours where n = 20.

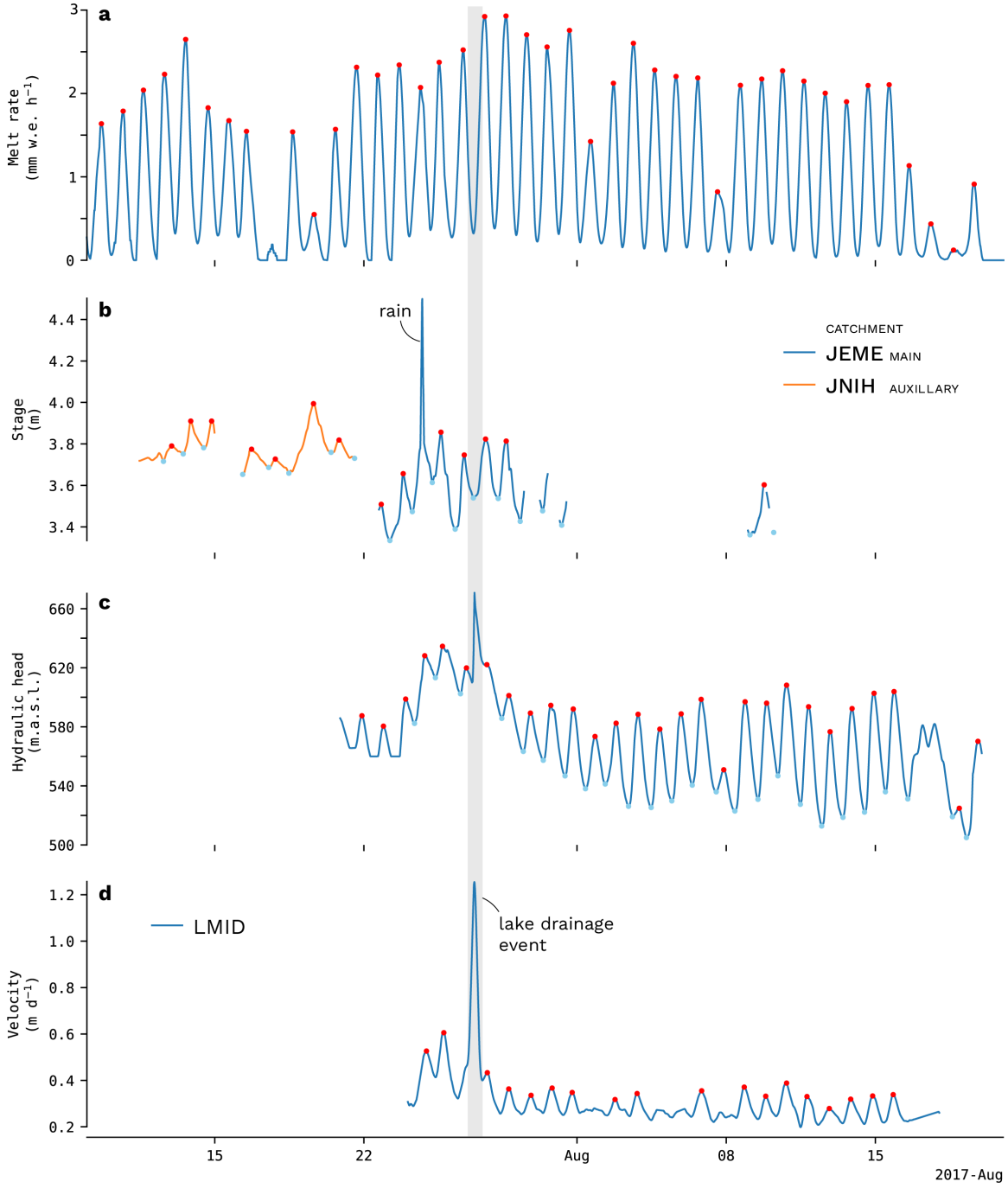

Figure S9. Low Camp 2017 timeseries and extrema picks. (a) Melt rate with diurnal maxima marked in red. (b) Supraglacial stream stage for our auxiliary catchment JNIH (orange) and our main catchment JEME (blue). Diurnal maxima (red) and minima (light blue) are marked. The abrupt jump in stream stage corresponds to a rain event. Stream stage is determined from an arbitrary reference point due to lack of a continuous stream depth timeseries. (c) JEME moulin hydraulic head. Flat minima values on 21-23 July were caused by moulin water level dropping below the piezometer's submerged depth. Continued lowering on 24 July 2017 enabled measurements of the full range of diurnal variability. (d) Along-flow surface ice velocity from the LMID GNSS station. Gray shading marks the timeperiod associated with a rapid supraglacial lake drainage several kilometers upglacier of our study site (see Mejia et al., 2021, for a complete description of this event).

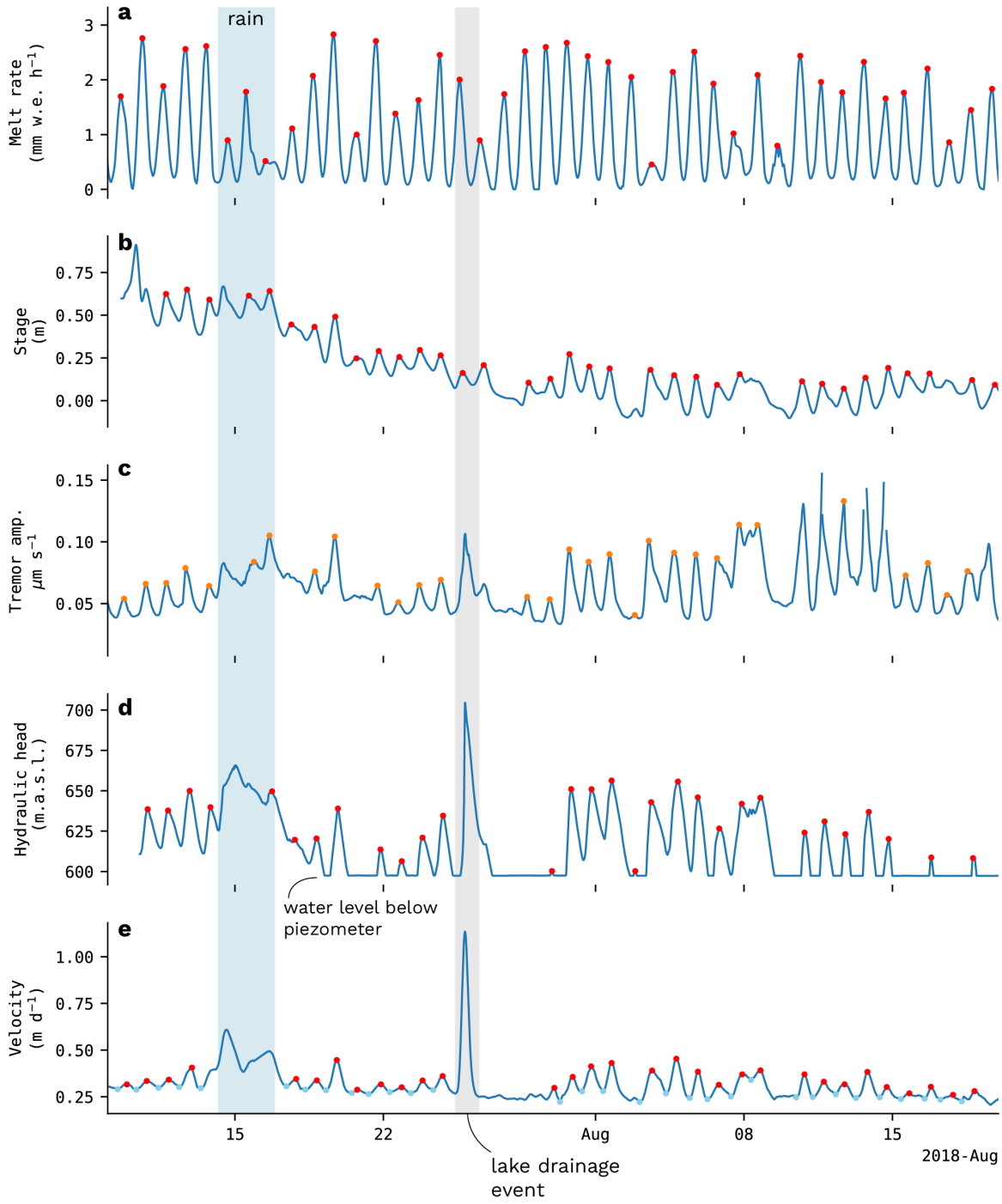

Figure S10. Low Camp 2018 timeseries and extrema picks. Similar to Figure S6 but for the 2018 melt season. (a) Surface melt rate with extrema picks. (b) PIRA stream stage. (c) PIRA hydraulic head. The flat lines mark the piezometer's elevation within the moulin shaft and indicate water levels dropping below the sensor. (d) Along-flow ice velocity from station LMID. Spikes in panels c–e on 25 July are a result of a subglacial flood-wave passing beneath our site (see Mejia et al., 2021, for a complete description of this event).

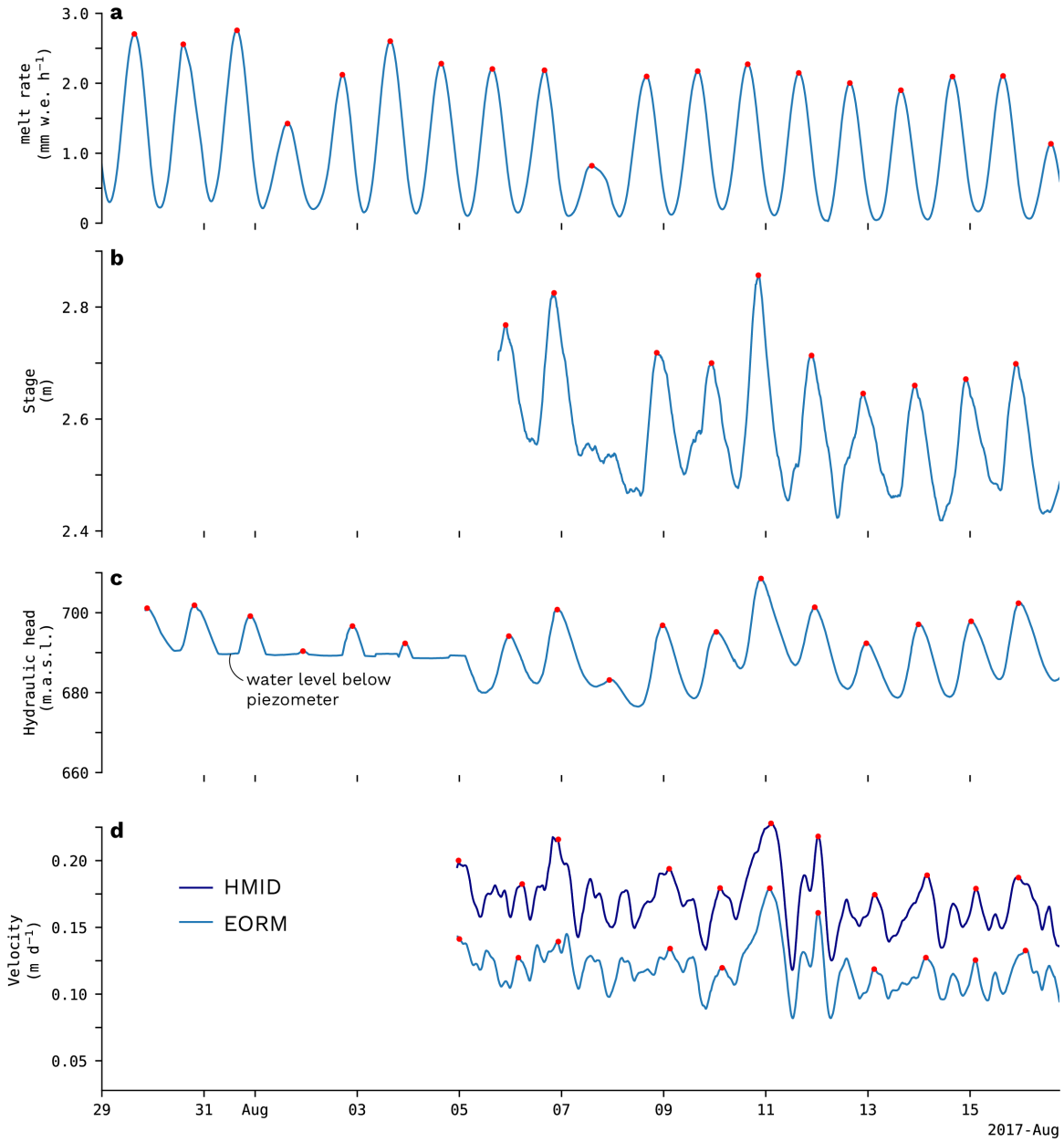

Figure S11. High Camp 2017 timeseries and extrema picks. (a) Melt rate with diurnal peaks (red). (b) Radical River supraglacial stream stage with respect to an arbitrary datum of 4 m. (c) Radical Moulin hydraulic head. The full range of diurnal moulin head oscillations was captured after the further lowering of the piezometer within RADI moulin on 5 August. (d) Along-flow ice velocity measured from stations HMID (purple) and EORM (blue). Diurnal peaks in ice velocity were confirmed with visual inspection of displacement timeseries.

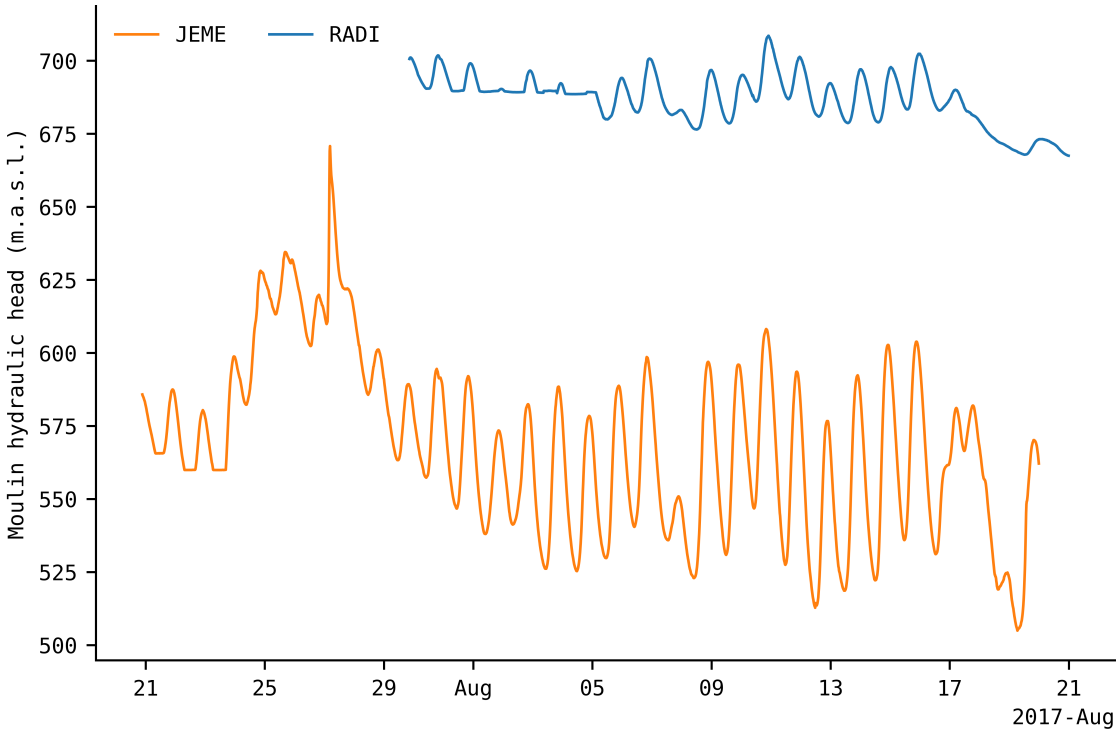

Figure S12. Moulin water level comparison. Measurements from Low Camp's JEME moulin (orange) and High Camp's RADI moulin (blue) plotted together on the same axis. The ice surface at Low Camp is 765.8 m.a.s.l. and the ice is approximately 503 m thick. The ice surface at High Camp is 933.2 m.a.s.l. and the ice is approximately 712 m thick.

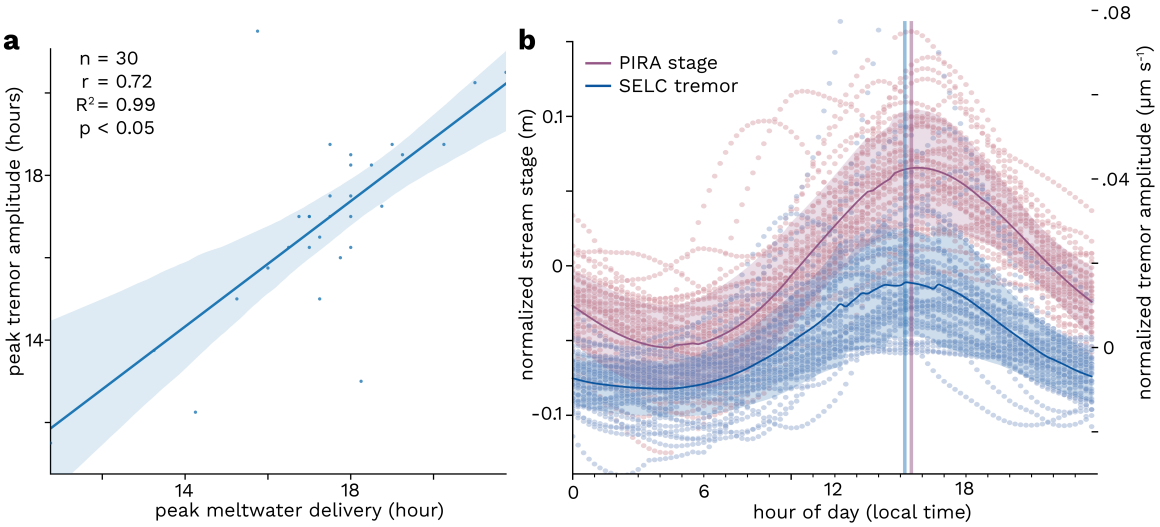

Figure S13. Glacio-hydraulic tremor and meltwater delivery relationship, Low Camp 2018. (a) Peak timing correlation between the time (decimal hours) of peak meltwater delivery to moulin PIRA, and the time of peak tremor amplitude. Blue line shows a linear regression between the two values with the standard deviation confidence interval shaded in blue. Annotations describe ordinary least squares correlation R^2=0.99 and p-value < 0.05 and the Pearson correlation coefficient (r=0.72). (b) Normalized diurnal fluctuations for stream stage (purple, left axis) and tremor amplitude (blue, right axis). Average values and the associated standard deviation from the mean are plotted, with the average peak meltwater delivery (15:30 UTC-02:00), and peak tremor amplitude (15:15 UTC-02:00) indicated with vertical lines.

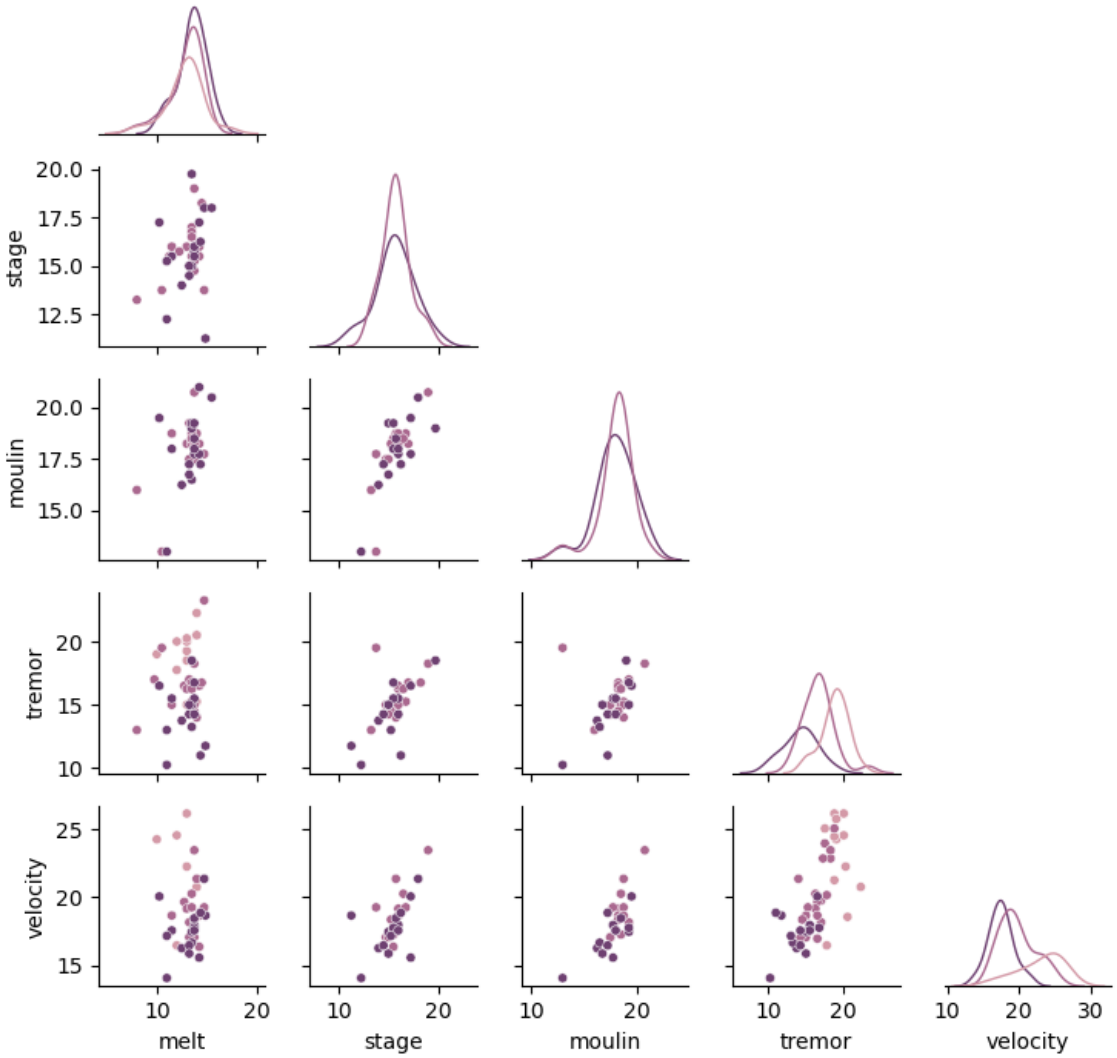

Figure S14. Low Camp 2018, correlation between variables and monthly comparison. Colors correspond to values from June (pink), July (light purple), and August (purple).